Alkali Metal Assisted Synthesis of Graphite Carbon Nitride with Tunable Band-Gap for Enhanced Visible-Light-Driven Photocatalytic Performance

Wenjun Wang [a, 1], Piao Xu [a, 1], Ming Chen [a,1], Guangming Zeng [a, *], Chen Zhang [a, *], Chengyun Zhou [a], Yang Yang [a], Danlian Huang [a], Cui Lai [a], Min Cheng [a], Liang Hu [b], Weiping Xiong [a], Hai Guo [a], Man Zhou [a]

a *College of Environmental Science and Engineering, Hunan University and Key Laboratory of Environmental Biology and Pollution Control (Hunan University), Ministry of Education, 8 South Lushan Road, Yuelu District, Changsha 410082, P.R. China*

b *School of Minerals Processing and Bioengineering, Central South University and Key Laboratory of Biohydrometallurgy (Central South University, Ministry of Education, 932 South Lushan Road, Yuelu District, Changsha 410083, P.R. China*

[*] Corresponding authors at: College of Environmental Science and Engineering, Hunan University, Changsha 410082, PR China.

E-mail addresses: zgming@hnu.edu.cn (G. Zeng), zhangchen@hnu.edu.cn (C. Zhang).

[1] These authors contribute equally to this article.

Abstract

The development of high-performance semiconductor photocatalysts using solar energy has become a hot topic, which is crucial for a sustainable future. However, construction of a non-toxic and efficient catalyst still remains an enormous challenge. Here, we uncover a simple hydrothermal re-calcination method to prepare a novel potassium (K) doped porous ultrathin g-C_3N_4 (denoted as KMCN) photocatalyst with efficient catalytic performance, eco-friendly characteristics and excellent stability. The obtained KMCN nanosheets were applied to the photo-degradation of tetracycline (TC) under different reaction condition to simulate practical wastewater treatment. It was found that porous structure and K^+ addition of g-C_3N_4 enhanced pores size and specific surface area (SSA), and increased the photo-absorption region and activity sites. The optical properties of KMCN nanosheets were systematically characterized by PL, UV-DRS, etc. The results revealed that KMCN (0.05) sample possessed narrowed band-gap, lower recombination of photo-generated charges and higher electrons and holes transfer efficiency. Benefiting from these advantages, KMCN (0.05) photocatalysts demonstrated excellent photocatalytic performance for TC degradation (85.13%), which was approximately 2.88-fold and 1.40-fold increase compared to bare g-C_3N_4 (29.60%) and porous ultrathin g-C_3N_4 (60.84%), respectively. These results suggest a reasonable way for the design of economic and high-efficiency photocatalysis.

Keywords

Porous g-C_3N_4; Photocatalysis; Potassium doped; Tetracycline; Nanostructures

INTRODUCTION

Energy crisis and environmental pollution have turn into the two stumbling blocks to achieve sustainable development in modern society.[1-8] Among them, the problems related to the antibiotic wastewater pollution are arrived an urgent level which threaten the survival of plants and animals.[9-16] Tetracycline (TC) was regarded as an essential medicine by the World Health Organization (WHO), which has been widely applied in animal husbandry and aquaculture.[17] However, TC was poorly metabolized in animals, which would result in prodrug or metabolite of TC entered into aqueous systems. Based on the continuous efforts of researchers, numerous traditional methods including chemistry flocculation, biology membrane filtration and physics adsorption method were applied to solve practical antibiotic wastewater problems.[18-23] However, it is quite tough to obtain ideal effects based on those methods because of complex process, secondary pollution and enormous cost.[24] Hence, convenient, non-toxic and effective solutions for antibiotic wastewater treatment are urgently desired for the development of our society.

Solar energy is an inexhaustible and clean energy in contrast to non-renewable energy like fossil energy in the world. In recent few decades, owing to the characteristics of economic and environment friendly, semiconductor photocatalysis technology driven by solar energy has become a research focus and been well employed in wastewater treatment.[25-27] From previous studies, it is noted that visible light driven photocatalyst is vital for photo-degradation reaction. As traditional photocatalyst, TiO_2 and ZnO are widely researched because of their nontoxicity and

high chemical stability, but been still restricted by their wide band-gap and only UV-excited property.[28-31] Therefore, to maximize the utilization of solar power and probe visible light driven photocatalysts has aroused widespread concern.

As a conjugated polymer semiconductor, g-C_3N_4 has recently triggered considerable attention own to its appealing electronic structure, excellent physicochemical stability, and proper band-gap (~2.7 eV).[32] The high condensation degree and heptazine ring structure enable g-C_3N_4 to obtain the above advantages, and those distinct properties further make g-C_3N_4 a prospective candidate for visible light driven photocatalysts.[33] Early in 2009, Wang and his co-workers[34] creatively employed g-C_3N_4 to generate hydrogen by using visible light irradiation. Since then, numerous g-C_3N_4 with good chemical and thermal stability were prepared via facile polymerization of earth-abundant low material such as melamine,[32] urea,[35] cyanamide,[36] dicyandiamide,[37] and thiourea.[38] Nonetheless, the photocatalytic efficiency of pure g-C_3N_4 is restricted by its ultrafast recombination of light-induced e/h^+, small specific surface area (SSA) and limited visible light absorption. Fortunately, many attempts including element doping,[39] morphology modulation,[40] band structure engineering,[40] thickness control[35, 41] and build g-C_3N_4 based heterojunction[42] were proposed to solve these shortcomings. Among them, forming the porous nanostructure of g-C_3N_4 seems to be an effective way because porous g-C_3N_4 not only can offer readily access channels to shorten the diffusion path of photo-induced charges from the interior to the surface, but also can increase the number of surface available active sites for photocatalysis reactions. Wang and his

co-workers[43] prepared ordered mesoporous g-C_3N_4 via using SBA-15 as hard template, and as-obtained products showed outstanding photocatalytic activity in the degradation of ciprofloxacin (CIP). But the hard template method preparation of porous carbon nitride will certainly cause pollution to the ambient environment. Besides, the photocatalysis efficiency and the separation of charges of porous g-C_3N_4 need further improvement to a significantly level. The element doped g-C_3N_4 photocatalysts present the enhanced photocatalytic activity because of its unique electronic structure which can effectively enhance charge carrier separation, as well as its narrowed band gap which can exhibit better optical property. More recently, metal elements (alkali metal and transition metal) and nonmetal elements (P, S, O, N or C) have been employed to modify porous g-C_3N_4.[44-49] According to previous reports, K doped g-C_3N_4 possesses bridge of the layers and photo-generated electron-hole pair delivery channels, which were caused by K atom bridged with other atom at the adjacent two layers.[50] It should be noted that the combined strategies (element doping in porous g-C_3N_4) have synergistic effect to further enhance the photocatalytic performance.

Motivated by the above studies, our present work used the combined strategy to prepare K doped porous g-C_3N_4. At first, porous ultrathin g-C_3N_4 was synthesized by the thermal polymerization of urea and melamine, the role of urea was acted as a soft template to generate porous structure. Then, a facile hydrothermal re-calcination method was applied to synthesize K doped MCN, and the as-obtained photocatalysts exhibited highly enhanced performance for TC removal compared to bare g-C_3N_4.

Herein, the mechanisms of K doping were analyzed, and the characteristics of the KMCN photocatalysts were also illustrated. It is fascinating to note that K^+ intercalated porous g-C_3N_4 possesses various favorable properties, such as the promoted pore size and SSA, as well as the improved efficiency of charge transport and better optical property. Introduced K^+ into the g-C_3N_4 interlayer can shifted the position of valence band, extend the π conjugated system and modulate the electronic structure, which would lead to the facilitated light-harvesting ability and suppressed recombination of charge carriers. Furthermore, the appropriate KOH concentration could increase SSA and reduce the crystal size. This treatment may open up a new avenue on designing highly efficient g-C_3N_4 photocatalysts through this combined strategy.

EXPERIMENTAL SECTION

Reagents. Melamine ($C_3N_3(NH_2)_3$), urea ($CO(NH_2)_2$), potassium hydroxide (KOH), sodium oxalate ($Na_2C_2O_4$), isopropanol (IPA), poly (vinyl alcohol) (PVA) 4-hydroxy-2,2,6,6-tetramethylpiperidinyloxy (TEMPOL) and tetracycline (TC) were purchased from Sinopharm Chemical Reagent Co., Ltd (Shanghai, China). In this study, all chemicals and materials were analytical grade and were used without additional treatments.

Synthesis of the catalysts. In a typical synthesis process, bare g-C_3N_4 was prepared via calcination of melamine (6.00 g) at 550 ℃ for 4 h with a ramp rate of 2.3 ℃/min. A yellow g-C_3N_4 sample was obtained after natural cooling to room

temperature.

The ultrathin porous g-C_3N_4 (MCN) was prepared by a precursor-reforming strategy with minor modifications.[35] Firstly, urea (8.56 g) and melamine (6.00 g) were dissolved in 30 mL de-ionized water, respectively, and then mixed the melamine and urea solution. The resulting suspension was stirred for 1 h. In fact, urea can provide a gas template and acts as a porogen, promoting the formation of porous g-C_3N_4. Subsequently, the precipitate was transferred to a 100 mL autoclave and the autoclave was heated at 180 ℃ for 1 d. After that, the intermediate product was obtained and washed several times with ethanol and deionized water and dried in the oven. Finally, the product was milled into power and calcined at 550 ℃ to acquire MCN.

In a typical experiment, a certain amount (0.30 g) MCN was added into 10 mL de-ionized water, and mixing 10 mL KOH solution (0.02, 0.05, 0.1 and 0.2 M) under stirring. Then, this mixture solution dried at 80 ℃ overnight to remove liquid. The obtained products were centrifugated and washed with de-ionized water to clean residual product. The solid product was followed by grinding and calcination in a corundum crucible at 550 ℃ for 4 h with a ramp rate of 2.3 ℃/min. The final product was denoted as KMCN (x), where x represents the concentration of KOH. For comparison, MCN was dispersed into 20 mL deionized water following the same procedure as in the synthesis of KMCN (0).

Characterization. The crystal phase of catalysts was analyzed by D8 Advance X-ray diffraction (XRD) with Cu Kα radiation in the region of 2θ from 10 º to 80 º. FT-IR spectra were obtained on Bruker spectrometer over the frequency range

4000-450 cm^{-1}. XPS measurement was recorded on Escalab 250Xi spectrometer with an Al Kα X-ray source. The UV-DRS were carried out on an Cary 300 UV-Vis spectrophotometer in the wavelength range from 200 nm to 800 nm. The morphologies of the catalysts were acquired using an atomic force microscopy (AFM), transmission electron microscopy (TEM) and scanning electron microscopy (SEM). The PL spectra were acquired from Fluoromax-4 spectrofluorometer under excitation wavelength of 340 nm. ESR signals of radical were collected on JEOL JES-FA200 spectrometer. The three-dimensional excitation-emission matrix fluorescence spectra (3D EEMs) were collected on fluorescence spectrophotometer (LS55, PerkinElmer), the corresponding emission wavelength (λ_{em}) and excitation wavelength (λ_{ex}) were 300-550 nm and 200-450 nm.

Photocatalytic activity. The light source was a 300 W Xe lamp (PLS-SXE 300). The photocatalytic performance of the KMCN(x) was tested by the visible light degradation of TC at ambient temperature. And the light density parameter was 0.33 W/cm^2, which was measured by PL-MW2000 photoradiometer. Typically, 30.00 mg sample was added into 30 mL TC (20 mg/L) solution. To establish the adsorption–desorption equilibrium before visible light irradiation, this solution was churned for 0.5 h in the condition of dark. The concentrations of TC were recorded by UV-Vis spectrophotometer with absorbance at its characteristic absorption peaks (357 nm).

Identification of degradation intermediates. The photo-degradation intermediate products of tetracycline were determined by LC-MS/MS system. In this work, the elution was made up by 0.1% (v/v) acetonitrile (C_2H_3N) and formic acid

(HCOOH). The linear gradient elution was set as follows: from 90% formic acid and 10% acetonitrile to 10% formic acid and 90% acetonitrile within 10 min and maintained 4 min. Then, this elution was adjusted to the initial conditions (90% formic acid and 10% acetonitrile) within 2 min and kept 2 min. Mass spectra (MS) was analyzed by electrospray ionization (ESI) source in the positive ionization mode, and MS was scanned by mass between m/z 210-500.

Electrochemical measurements. The photoelectrochemical tests of as-prepared samples were analyzed by a CHI0-660D workstation (Shanghai Chenhua Instrument Co., Ltd., China). Ag/AgCl electrode acted as the reference electrode, and Pt electrode was used as the counter electrode. The working electrodes were fluorine-doped tin oxide (FTO) loaded with 100 μL sample. Specific load process was as follows: Firstly, FTO was cleaned with acetone, ethanol and deionized water via sonication method. Secondly, 8 mg sample was dispersed evenly in 150 uL PVA. Finally, 100 uL suspension was dropped onto FTO and heated in a vacuum oven for 1.5 h at 150 ℃. In addition, the 300 W xenon lamp with a cutoff filter was regarded as light source, and 0.2 M Na_2SO_4 aqueous solution was used as electrolyte in this three-electrode system.

RESULTS AND DISCUSSION

Crystal phase. The formation of potassium (K) doped carbon nitride was proved by XRD, XPS and FT-IR spectroscopy. The XRD patterns of bulk g-C_3N_4, MCN and KMCN (x) were depicted in Figure 1a. The as-prepared samples showed two diffraction peaks at around 13.1 °(100) and 27.2 °(002), which could be attributed to

the in-planar structural packing and characteristic inter-planar stacking peaks of typical graphite-like carbon nitride.[32, 51] Compared to pure g-C_3N_4, the crystal phase of MCN and KMCN (x) did not change with the porous structure and potassium addition, indicating that no impurities were created in the preparation process. However, the intensities of two diffraction peaks of modified samples were lower and weaker, which might be ascribed to the defects caused by the incomplete polymerization.[44, 52]

Similarly, FT-IR spectrum of MCN, KMCN (x) and bulk g-C_3N_4 were presented in Figure 1b. The spectrum of modified g-C_3N_4 was generally the uniform as that of the bulk one. The peak at about 800 cm^{-1} was assigned to the tri-s-triazine ring modes, which was consistent with previous findings.[53] Signals at about 1639 cm^{-1} can be correspond to the typical C=N stretching vibration mode, while the absorption band centered in the 1200-1600 regions can be assigned to typical stretching models of carbon and nitrogen heterocycles (C_6N_7).[44, 54] The wide peaks located at around 2900-3500 cm^{-1} are assigned to the hydrogen-bonding interactions, originating from N-H stretching.[55] It was noteworthy that the peak at about 3300 cm^{-1} tiny decreased after K doped and re-calcination, meaning the replace of H sites in amino groups by K^+ and formation of N-K bonding.[50] It should be believed that K^+ had been inserted into the orderly g-C_3N_4 framework and partly damage its framework based on the formation of N-K bonding, which was also in good accordance with the decreased (002) and (100) diffraction peak (Figure 1a).

The surface chemical compositions and electronic states of the bulk g-C_3N_4, MCN and KMCN (0.05) were performed by XPS measurement (Figure 2). As illustrated in Figure 2a, N, C, O and K elements can be found in the full survey spectrum of KMCN (0.05) sample, but the K peak was not obvious because of low concentration in the sample. The small amount of oxygen might be originated from the polymerization process of g-C_3N_4 and the oxygen from water or KOH.[56-57] For the C 1s region, the two peaks seated at 288.4 eV and 284.8 eV. And the former was attributed to the sp^2 carbon (N-C=N) in N-containing aromatic rings of g-C_3N_4. The latter was assigned to alkyl (C==C-C or C-H), which derived from bulk g-C_3N_4 formed during decomposition.[32, 58-59] The N 1s peaks (Figure 2c) of MCN and bulk g-C_3N_4 could be divided into three sub peaks at about 400.9 eV, 399.5 eV and 398.8 eV, which belonged to the surface N-H, hybridized sp^3N with bonding hydrogen and C-N-C, respectively. Notably, the two peaks at about 400.9 eV and 399.5 eV disappeared in KMCN (0.05) after K^+ modification, and formed a new peak about at 400.7eV (C-N_3).[50] This fact shows the deprotonation effect of K doped g-C_3N_4 and the substitution of H atom in amino groups by K atom.[50, 60-61] Furthermore, the XPS spectrum of K 2p was depicted in Figure 2d. The binding energies located at 295.2 eV and 292.8 eV were consistent to the K $2p_{1/2}$ and K $2p_{3/2}$ peaks of K in KMCN (0.05), suggesting that K is successfully doped into g-C_3N_4 and formation of the N-K chemical bond.[44]

Morphology and microstructure. The morphology and microstructure of bulk g-C_3N_4, MCN and KMCN (0.05) were examined by SEM, and the corresponding

images are displayed in Figure 3. Bulk g-C_3N_4 (Figure 3a) displays an aggregated, chunky and crystals stacking with smooth structures, which is consistent with previous research.[62] Furthermore, the addition of urea that acts as a porogen, allowing the simple preparation of porous g-C_3N_4 with rough and stacking pimple-like structure (Figure 3b). After the process of K doping and re-calcination, a rougher structure and porous can be seen in Figure 3c. Energy dispersive spectroscopy (EDS) elemental mapping images displayed a neat distribution of N, C and K under the surface of KMCN (0.05), which confirmed the existence of K species in KMCN (0.05) (Figure 3d-f). The detailed crystal phase of the obtained samples was further observed by TEM. As depicted in Figure 3g, pure g-C_3N_4 presented a smooth and amorphous structure with no pores on its surface. The thinner and more transparent sample of MCN was depicted in Figure 3h, one can clearly see the nanosheets with randomly distributed porous. The structure of KMCN (0.05) exhibited many microporous and macroporous, at approximately 5-40 nm (Figure 3i). These observed results are highly agreeing with the SEM observation. In addition, K was successfully doped MCN was also verified by the typical EDS spectrum of TEM (Figure S1).

To further study the increased SSA and pores characteristic of MCN, KMCN (0.05) and bulk g-C_3N_4, the N_2 adsorption-desorption isotherms experiments have been investigated, and the results were shown in Table 1 and Figure 4. The pore-size distribution of the photocatalysts was also estimated and performed (see the inset of Figure 4). As depicted in Table 1, the SSA of bulk g-C_3N_4, MCN, KMCN (0), KMCN (0.02), KMCN (0.05), KMCN (0.1) and KMCN (0.2) were calculated to be 12.735,

26.566, 29.314, 34.155, 50.196, 42.792 and 40.983 m^2/g, respectively. Obviously, the KMCN (0.05) sample obtained the highest SSA among all samples. The SSA, pore volume and pore size of KMCN (0.05) is approximately 3.9-times, 4.4-times and 1.4-times of bulk g-C_3N_4, respectively. Larger specific area and enhanced pore volume of KMCN (0.05) might provide more reaction sites for the pollutants and promoted the photocatalytic activity rather than the adsorption ability. Atomic force microscopy (AFM) image (Figure S2) indicates an average thickness of 3.2 nm for the KMCN (0.05), which comprises about 7 ~ 8 atomic layers of g-C_3N_4. These results supported the TEM and further verified the successful preparation of MCN and KMCN (x), which has thin and porous nanosheets.

Optical property and band structure. The light absorption property and band structure could be used as a reference to evaluate optical property of samples. As showed in Figure 5a, the absorption regions of bulk g-C_3N_4 are at ~470 nm.[38] In contrast, MCN and KMCN (x) samples presented wider absorption in the visible light edges. This result indicated that modified g-C_3N_4 have enhanced visible light absorption ability. The band energy gap (E_g) of photocatalysts was also analyzed and shown in inset of Figure 5a. Generally, the E_g could be calculated by the following formula:

$$ahv = A(hv-E_g)^{n/2} \quad (1)$$

Where E_g, h, a, A and v are the band energy gap, Planck constant, absorption coefficient, a proportionality constant and light frequency, respectively. Among them, the value of n is 1 because of semiconductor's direct transition. Based on that, the E_g

is estimated to be 2.33 eV and 2.65 eV for KMCN (0.05) and bulk g-C_3N_4, respectively. The E_g of KMCN (0.05) is slight smaller than bulk g-C_3N_4, which fitted well with the enhanced light absorption. The CB and VB of as-prepared samples are further studied by VB-XPS spectra and Mott-Schottky method.[38, 63-64] The VB-XPS spectra of samples are described in Figure 5b. It suggested that the energy gaps of bulk g-C_3N_4 and KMCN (0.05) between Fermi level (E_f) and VB are 2.46 eV and 2.22 eV, respectively.[38] Figure 5c performs that the Mott-Schottky plots of KMCN (0.05) and bulk g-C_3N_4 to obtain flat band potential under the condition of 1000 Hz frequencies. Their flat band potentials are calculated to be -0.62 eV and -0.76 eV, versus the Ag/AgCl electrode. Thus, the numeric values are -0.42 eV and -0.56 eV versus the normal hydrogen electrode (NHE).[38, 63-64] Because the Fermi level was approximately equal to the flat band potentials for n-type semiconductors,[38, 63-64] the Fermi levels of KMCN (0.05) and bulk g-C_3N_4 are -0.56 eV and -0.42 eV, respectively. Consequently, the band structure of photocatalysts and positions of VB and CB are shown in Figure 5d.

Photoluminescence and photo electrochemical properties. Photoluminescence (PL) spectroscopy was applied to study photo-excited carries excitation, migration and recombination in photocatalysts, and its excitation wavelength was 340 nm (Figure 6). In general, lower PL signals present higher photo-induced carries separation efficiency.[65-66] Obviously, the PL intensities of KMCN (0.05) was lower than other samples, which illustrate that the recombination rate of light-excited e^-/h^+ pair was restrained by porous structure and K doping.

For better understanding the course of light-generated electron movement in the as-prepared samples, some other photoelectrochemical technologies like electrochemical impedance spectra (EIS) and photocurrent response measurement have been applied. The photocurrent response results (Figure 7a) of MCN, KMCN (0.05) and bulk g-C_3N_4 were repeatable and stable under visible light illumination. Furthermore, photocurrent response density of KMCN (0.05) shows the highest and enhanced about 3 times than bulk g-C_3N_4. EIS method is another technology to prove the separation efficiency of photo-generated charge. The smaller arc radius means higher separation efficiency of photocatalysts. Figure 7b presented the EIS Nyquist plots of corresponding samples, and the size of arc radius order is bulk g-C_3N_4 > MCN > KMCN (0.05), which reflects that the prepared K doped MCN catalysts shows a more efficient light-generated charge separation ability and faster interfacial charge migration skill. The equivalent circuit diagram (Figure S3) and the fitted electrical parameters (Table S1) were obtained from ZSimpWin software. The charge transfer resistances (R_{CT}) can be determined by the arc radius. As illustrated in Table S1, R_{CT} of bulk g-C_3N_4, MCN and KMCN (0.05) are 33100, 32000 and 28700 Ω, respectively. The evidently decreased resistance of the KMCN (0.05) means efficient interfacial charge separation process on the surface of the KMCN (0.05) electrode.

Photocatalytic activities. TC, a typical antibiotic, was chose as the target contaminant to test the as-prepared photocatalytic performance. The dark adsorption efficiency of photocatalysts was investigated before visible light irradiation (Figure S4). In addition, 0.5 h of dark adsorption was put into all the photodecomposition

reaction before visible light irradiation. Figure 8a showed the photodecomposition efficiency of TC with different photocatalyst components. It can be observed that all photocatalysts showed different photo-degradation efficiency, which was in a certain order of KMCN (0.05) > KMCN (0.1) > KMCN (0.2) > KMCN (0.02) > KMCN (0) > MCN > bulk g-C_3N_4. All of K doped MCN samples showed superior photodecomposition efficiency compared to MCN and bulk one, which caused by K^+ addition and porous structure.[35, 44, 50] The KMCN (0.05) catalyst exhibited the highest photocatalytic performance (85.13%) in 1 h light irradiation, which was ~2.88 times than bulk g-C_3N_4 photocatalytic activity (29.6%). However, excess K may act as the photo-carrier's recombination center and suppress the photocatalytic performance because of covered light adsorption.[35] As shown in Figure S5, other pollutants (ciprofloxacin and Rhodamine B) have also been tested by KMCN (0.05).

To deep study the photocatalytic activity, the experimental results were analyzed by pseudo-first-order kinetic model (Figure S6). It can be known that all of the samples conform to the pseudo-first-order kinetic model, expressed as the following formula:

$$\ln (C_t/C_0) = -K_{app}t \quad (2)$$

Where C_t and C_0 are TC concentrations at time t and 0 and K_{app} is the rate constant (min^{-1}), respective. Furthermore, degradation efficiencies (DE), standard error and the corresponding K_{app} for the TC in different samples are presented in Table 2. The K_{app} values of the KMCN (0.05) catalysts were the highest, which was about 4.86-fold higher than that of bulk g-C_3N_4 and 1.75-fold higher than MCN. Therefore, the

above-mentioned results demonstrated KMCN (0.05) possess optimum photocatalytic activity, which was consistent with the before characterization results. Various reaction conditions like initial TC concentration, supporting electrolytes and different irradiation conditions were also investigated for meeting practical application.

Effect of initial TC concentrations. Initial TC concentrations have a great influence on photocatalyst activities in practical application. Figure 8b showed the TC degradation with a series of initial TC concentrations (10, 20, 30 and 40 mg/L) by using KMCN (0.05) sample. It could be clearly detected that 92.06%, 85.13%, 70.77% and 62.62% of TC were removed at the initial TC concentration equal to 10, 20, 30 and 40 mg/L, respectively. In the photocatalytic oxidation process, higher initial contaminant may present stronger negative effect, which can result in less photons entering the reaction solution and decrease the reactive oxygen species on the surface of KMCN (0.05) catalysts.[67] Moreover, TC degradation products can compete with the TC molecules and occupy some reaction sites on the surface of photocatalysts, and more degradation intermediates will be produced under the condition of high concentration of pollutants.[68-69] Therefore, the results suggested that high TC removal was easy to obtain at low contaminant concentration.

Effect of supporting electrolytes. In real water applications, co-existing ions such as sulfate, chloride and carbonate ions will unavoidably affect photocatalytic activity and must take it into consideration. Further, the supporting electrolytes could act as radical scavengers and greatly influence the photocatalytic performance under visible light irradiation. Herein, sulfate, chloride and carbonate ions were put into

natural water to simulate real water for the purpose of TC removal by KMCN (0.05) nanosheets. Figure 8c displayed the results of TC photo-degradation with above supporting electrolytes at concentration of 0.05 M. Among them, the sodium salts shows an insignificant effect on the photo-degradation of TC.[67] As illustrated in Figure 8c, the three supporting electrolytes all have negative influence for the photocatalytic degradation efficiency, and the corresponding decreasing order as follows: carbonate > sulfate > chloride. Tiny decrease could be found within chloride, the reason for causing this result was mainly competitive adsorption activity sites between TC molecules and Cl^- on the surface of the photocatalyst. On the contrary, negative influence obviously existed in the presence of carbonate and sulfate on the light-degradation of TC. It has been studied that carbonate and sulfate can act as scavengers of hydroxyl radicals, which can greatly inhibit the photocatalytic efficiency of KMCN (0.05) photocatalysts.[42, 68] Therefore, the photocatalytic efficiency was influenced by the supporting electrolytes ions.

Effect of light irradiation condition. Solar energy always stands a key level in the photocatalytic field due to its abundance and easy accessibility. Thus, it is necessary to study the effect of light illumination conditions (dark, visible light and full spectrum) for the photocatalytic efficiency. As can be seen in Figure 8d, there was scarcely photolysis of TC without photocatalysts, which can indicate chemical stability of TC. On the contrary, almost all TC was degraded by KMCN (0.05) sample after 1 h under full spectrum illumination. Additionally, about 85.13% of TC could be removed under 1 h visible light irradiation. Simultaneously, it should be noted that the

shorter wavelength of the light can possess higher photons energy.[70] Under dark condition, removal of TC was ascribed to the adsorption process. The above results validated that KMCN (0.05) catalysts have great potential in the application of real wastewater treatment.

Mineralization of TC and stability of KMCN (0.05). The abilities of mineralization and stability are crucial for pollution removal of semiconductor photocatalysts. As described in Figure 9a, the degradation and mineralization for TC was analyzed by total organic carbon (TOC) analyzer. The decomposition and mineralization efficiency reached 87.98% and 25.45% for KMCN (0.05) sample within 2 h visible light irradiation. The results illuminated that KMCN (0.05) sample could validly mineralize TC into intermediate product or CO_2 and H_2O, which exhibited a promising photocatalyst for wastewater treatment. Furthermore, the chemical stability and reusability of KMCN (0.05), as a key issue for actual applications, was also discussed under the same reaction conditions. The photo-degradation efficiency (Figure 9b) of KMCN (0.05) after four times recycling remained about 84.01%, only lost about 1.12% compared to original efficiency. Moreover, the used sample was obtained after the centrifugation, washing and drying. The used photocatalyst was characterized by FT-IR, XRD, SEM and XPS analyzer, and the results were shown in Figure S7 and Figure S8. All results indicated that there was no obvious change between fresh and used KMCN (0.05).

3D EEMs analysis. For deeply investigate the TC mineralization process based on KMCN (0.05) photocatalyst, 3D excitation emission spectra technology was used.

Six samples mappings (Figure 10) were obtained under different condition of adsorption and photo-degradation. According to our previous studies,[69-70] two main peaks of $\lambda_{ex}/\lambda_{em}$ = (240-250 nm) / (435-450 nm) (fulvic acids peak) and $\lambda_{ex}/\lambda_{em}$ = (305-330 nm) / (430-450 nm) (humic acids peak) would be observed if TC began decomposition. As shown in Figure 10a and Figure 10b, there was no obvious fluorescence appeared in the process of dark adsorption, indicating that TC molecules were stable and refractory. However, two characteristic peaks obtained when TC molecules were removed by KMCN (0.05) nanocomposite under visible light irradiation. Furthermore, with the irradiation time increasing from 0.5 h to 1.5 h, the fluorescence intensity of the fulvic acids and humic acids were accumulated (Figure 10c-e). But as revealed in Figure 10f, the fluorescence intensity decreased to some extent when the irradiation time reached 2 h. This phenomenon caused by partial TC intermediates thorough degraded and convert into CO_2 and H_2O. Hence, the ability of mineralization and stability of KMCN (0.05) sample were verified.

Possible degradation pathway of TC. It is meaningful to investigate the possible intermediates and reasonable degradation pathway of TC. The TC intermediates were analyzed by LC-MS, and their corresponding MS spectra and possible structural information were presented in Figure S9 and Table S2, respectively. The primary product with mass-to-charge ratio (m/z) of 445 was consistent with the molecular weight of original TC. Based on the eight intermediates of TC and previous literatures, the two possible photo-degradation pathways (the cleavage of specific functional groups and the aromatic ring-opening reactions) were presented as

illustrated in Figure 11. On the one hand, the C=C in TC was attacked by •OH to produce TC 1 with m/z = 461. Similarly, the product TC 2 (m/z = 477) appeared since the TC 1 was continuously attacked by •OH. Subsequently, the generation of TC 3 (m/z = 449) could be assigned to N-demethylation process owe to the low energy of N-C bond.[71] On the other hand, the TC 4 (m/z = 417) was produced via similar N-dealkylation process.[72] TC 5 with m/z value of 401 was stemmed from TC 4 since H_2O_2 attacks the hydroxyl group (-OH) at the C6 position in TC 4. Owing to cleavage of the carboatomic ring of TC 5, the product TC 6 (m/z = 333) was found in MS spectra.[73] Further photo-degradation of TC 6 led to the generation of TC 7 (m/z = 289) and TC 8 (m/z = 245) via decarboxylation process. In brief, above transformation intermediates resulted from three parts: hydroxylation, loss of some groups such as carboxyl, hydroxyl and N-methyl; cleavage of carboatomic ring. Moreover, the produced intermediates will be completely decomposed to H_2O, CO_2, NH_4^+, NO_3^-.[74]

Degradation mechanism analysis. In order to identify the predominant reactive species of KMCN (0.05), the main active species trapping experiments were completely studied. In this paper, three scavengers, IPA, TEMPOL and $Na_2C_2O_4$ were added in the photocatalysis reaction process and act as quenchers of •OH, $•O_2^-$ and h^+, respectively. As depicted in Figure 12a and Figure 12b, the photocatalytic activity was greatly inhibited by TEMPOL and the decomposition rate of TC reduced from 85.13% to 32.72%, which showed that $•O_2^-$ was the main reactive species of KMCN (0.05) sample. Meanwhile, the addition of 10 mM of $Na_2C_2O_4$ had middling effect and 10 mM of IPA had least effect on the photo-degradation of TC, indicating that h^+ also

played a dominated role and •OH radical played a second important role in photocatalytic degradation of TC for KMCN (0.05) photocatalyst.

For further investigated the roles of $•O_2^-$ radical and •OH radical, the ESR spin-trapping technology was performed on illuminates KMCN (0.05) nanocomposite. As depicted in Figure 12c and Figure 12d, there were no obvious signals in the blank condition. However, a stronger intensity signals can be found under the 4 and 8 minutes of visible light illumination. Therefore, the •OH and $•O_2^-$ radicals were produced during the photo-degradation process.

Based on the aforementioned analyses and these experimental results, a reasonable mechanism for TC photo-degradation over KMCN (0.05) nanocomposite was proposed (Scheme 1). It had been confirmed that K^+ was inset into porous ultrathin g-C_3N_4 through XRD, FT-IR and XPS and porous structure and K^+ addition plays an important role for the photoactivity enhancement. As shown in Scheme 1, the KMCN (0.05) photocatalyst can be easily excited and generate h^+ in the VB and e^- in the CB. The accumulation electrons on the CB could efficiently induce O_2 to generate $•O_2^-$, because the CB edge potential of KMCN (0.05) (-0.53 eV) was more negative than the reduction potential of $O_2/•O_2^-$ (-0.33 eV vs NHE).[32, 67] However, the VB potential of KMCN (0.05) was also more negative than the standard redox potential of $OH^-/•OH$ (2.40 eV vs NHE),[67] so the •OH radicals cannot be produced through the photo-generated holes oxidize H_2O. The obtained •OH maybe produced via H_2O_2 decompose.[75-76] The concentration of H_2O_2 was detected via the test paper, and the result was shown in Figure S10. Moreover, the holes on the VB of KMCN (0.05) also

made contribution to the degradation of TC. In conclusion, $\bullet O_2^-$, •OH and h^+ and radicals all joined in the photo-degradation process of TC into micromolecules and enhanced photocatalytic performance, which was fitted well with ESR analysis and the main active species identified in trapping experiment. The reaction process can be described as following equations:

$$KMCN\ (0.05) + hv \longrightarrow KMCN\ (0.05)\ (h^+ + e^-) \quad (3)$$

$$O_2 + e^- \longrightarrow \bullet O_2^- \quad (4)$$

$$\bullet O_2^- + e^- + 2H^+ \longrightarrow H_2O_2 \quad (5)$$

$$H_2O_2 + e^- \longrightarrow OH^- + \bullet OH \quad (6)$$

$$h^+, \bullet O_2^- \text{ and } \bullet OH + TC \longrightarrow \text{degradation products } (CO_2, H_2O \text{ etc}) \quad (7)$$

CONCLUSIONS

In summary, a novel K doped porous ultrathin g-C_3N_4 was prepared via a simple hydrothermal re-calcination approach. Owing to wider photo-absorption region and higher light-generated charges transfer efficiency, KMCN (0.05) nanocomposite exhibited outstanding photocatalytic performance for TC degradation. KMCN (0.05) sample showed 85.13% removal efficiency of TC, which was ~1.40-fold and 2.88-fold increase compared to MCN (60.84%) and bulk g-C_3N_4 (29.60%), respectively. Moreover, KMCN (0.05) also presented great chemical stability and mineralization ability, which was confirmed by analysis of TOC, 3D EEMs spectra and cycle experiment results. Furthermore, the possible decomposition intermediates of TC were analyzed by LC/MS-MS results. ESR analysis and active species trapping experiments manifested that $\bullet O_2^-$ and h^+ played a dominated role and •OH played a

second important role in TC photocatalytic degradation process. Our work shed light on the photocatalysis mechanism based on K^+ intercalated porous ultrathin g-C_3N_4, and might provide a new clue to design visible light excited photocatalysts for meet practical antibiotic wastewater treatment.

ASSOCIATED CONTENT

Supporting Information

TEM EDS spectrum, AFM, Equivalent circuit diagram, Adsorption ability and Pseudo-first-order kinetics of the prepared samples; XPS, XRD, SEM and FT-IR of used samples and prepared samples; The structural information of the possible intermediates products; The concentration of H_2O_2.

AUTHOR INFORMATION

Corresponding Authors

*E-mail: zgming@hnu.edu.cn (G.M. Zeng). Tel.:+86-731-88822754.

*E-mail: zhangchen@hnu.edu.cn (C. Zhang). Tel.:+86-731-88823701.

ORCID

Guangming Zeng: 0000-0002-4230-7647

Chen Zhang: 0000-0002-3579-6980

Acknowledgements

This study was financially supported by the Program for the National Natural Science Foundation of China (51709101, 51579098, 51779090, 51278176, 51408206, 51521006, 51378190, 51508177), the National Program for Support of Top-Notch Young Professionals of China (2014), Hunan Provincial Science and Technology Plan

Project (No.2016RS3026, 2017SK2243), the Program for Changjiang Scholars and Innovative Research Team in University (IRT-13R17)，and the Fundamental Research Funds for the Central Universities (531107051080, 531107050978, 531107051161).

References

1. Chen, M.; Xu, P.; Zeng, G.; Yang, C.; Huang, D.; Zhang, J., Bioremediation of soils contaminated with polycyclic aromatic hydrocarbons, petroleum, pesticides, chlorophenols and heavy metals by composting: Applications, microbes and future research needs. *Biotechnol. Adv.* **2015,** *33* (6), 745-755, DOI 10.1016/j.biotechadv.2015.05.003.

2. Zhang, C.; Lai, C.; Zeng, G.; Huang, D.; Yang, C.; Wang, Y.; Zhou, Y.; Cheng, M., Efficacy of carbonaceous nanocomposites for sorbing ionizable antibiotic sulfamethazine from aqueous solution. *Water Res.* **2016,** *95*, 103-112, DOI 10.1016/j.watres.2016.03.014.

3. Liang, J.; Yang, Z.; Tang, L.; Zeng, G.; Yu, M.; Li, X.; Wu, H.; Qian, Y.; Li, X.; Luo, Y., Changes in heavy metal mobility and availability from contaminated wetland soil remediated with combined biochar-compost. *Chemosphere* **2017,** *181*, 281-288, DOI 10.1016/j.chemosphere.2017.04.081.

4. Wu, H.; Lai, C.; Zeng, G.; Liang, J.; Chen, J.; Xu, J.; Dai, J.; Li, X.; Liu, J.; Chen, M.; Lu, L.; Hu, L.; Wan, J., The interactions of composting and biochar and their implications for soil amendment and pollution remediation: a review. *Crit. Rev. Biotechnol.* **2017,** *37* (6), 754-764, DOI 10.1080/07388551.2016.1232696.

5. Wan, J.; Zeng, G.; Huang, D.; Hu, L.; Xu, P.; Huang, C.; Deng, R.; Xue, W.; Lai, C.; Zhou, C.; Zheng, K.; Ren, X.; Gong, X., Rhamnolipid stabilized nano-chlorapatite: Synthesis and enhancement effect on Pb-and Cd-immobilization in polluted sediment. *J. Hazard. Mater.* **2018,** *343*, 332-339, DOI 10.1016/j.jhazmat.2017.09.053.

6. Ren, X.; Zeng, G.; Tang, L.; Wang, J.; Wan, J.; Liu, Y.; Yu, J.; Yi, H.; Ye, S.; Deng, R., Sorption, transport and biodegradation - An insight into bioavailability of persistent organic pollutants in soil. *Sci. Total Environ.* **2018,** *610*, 1154-1163, DOI 10.1016/j.scitotenv.2017.08.089.

7. Cheng, M.; Zeng, G.; Huang, D.; Lai, C.; Xu, P.; Zhang, C.; Liu, Y.; Wan, J.; Gong, X.; Zhu, Y., Degradation of atrazine by a novel Fenton-like process and assessment the influence on the treated soil. *J. Hazard. Mater.* **2016,** *312*, 184-191, DOI 10.1016/j.jhazmat.2016.03.033.

8. Cheng, M.; Zeng, G.; Huang, D.; Lai, C.; Liu, Y.; Zhang, C.; Wang, R.; Qin, L.; Xue, W.; Song, B., High adsorption of methylene blue by salicylic acid–methanol modified steel converter slag and evaluation of its mechanism. *J. Colloid Interface Sci.* **2018,** *515*, 232-239, DOI 10.1016/j.jcis.2018.01.008.

9. Gong, J.-L.; Wang, B.; Zeng, G.-M.; Yang, C.-P.; Niu, C.-G.; Niu, Q.-Y.; Zhou, W.-J.; Liang, Y., Removal of cationic dyes from aqueous solution using magnetic multi-wall carbon nanotube nanocomposite as adsorbent. *J. Hazard. Mater.* **2009,** *164* (2-3), 1517-1522, DOI 10.1016/j.jhazmat.2008.09.072.

10. Xu, P.; Zeng, G. M.; Huang, D. L.; Feng, C. L.; Hu, S.; Zhao, M. H.; Lai, C.; Wei, Z.; Huang, C.; Xie, G. X.; Liu, Z. F., Use of iron oxide nanomaterials in wastewater

treatment: A review. *Sci. Total Environ.* **2012,** *424*, 1-10, DOI 10.1016/j.scitotenv.2012.02.023.

11. Tang, W.-W.; Zeng, G.-M.; Gong, J.-L.; Liang, J.; Xu, P.; Zhang, C.; Huang, B.-B., Impact of humic/fulvic acid on the removal of heavy metals from aqueous solutions using nanomaterials: A review. *Sci. Total Environ.* **2014,** *468*, 1014-1027, DOI 10.1016/j.scitotenv.2013.09.044.

12. Tan, X.; Liu, Y.; Zeng, G.; Wang, X.; Hu, X.; Gu, Y.; Yang, Z., Application of biochar for the removal of pollutants from aqueous solutions. *Chemosphere* **2015,** *125*, 70-85, DOI 10.1016/j.chemosphere.2014.12.058.

13. Deng, J.-H.; Zhang, X.-R.; Zeng, G.-M.; Gong, J.-L.; Niu, Q.-Y.; Liang, J., Simultaneous removal of Cd(II) and ionic dyes from aqueous solution using magnetic graphene oxide nanocomposite as an adsorbent. *Chem. Eng. J.* **2013,** *226*, 189-200, DOI 10.1016/j.cej.2013.04.045.

14. Long, F.; Gong, J.-L.; Zeng, G.-M.; Chen, L.; Wang, X.-Y.; Deng, J.-H.; Niu, Q.-Y.; Zhang, H.-Y.; Zhang, X.-R., Removal of phosphate from aqueous solution by magnetic Fe-Zr binary oxide. *Chem. Eng. J.* **2011,** *171* (2), 448-455, DOI 10.1016/j.cej.2011.03.102.

15. Xu, P.; Zeng, G. M.; Huang, D. L.; Lai, C.; Zhao, M. H.; Wei, Z.; Li, N. J.; Huang, C.; Xie, G. X., Adsorption of Pb(II) by iron oxide nanoparticles immobilized Phanerochaete chrysosporium: Equilibrium, kinetic, thermodynamic and mechanisms analysis. *Chem. Eng. J.* **2012,** *203*, 423-431, DOI 10.1016/j.cej.2012.07.048.

16. Hu, L.; Wan, J.; Zeng, G.; Chen, A.; Chen, G.; Huang, Z.; He, K.; Cheng, M.;

Zhou, C.; Xiong, W., Comprehensive evaluation of the cytotoxicity of CdSe/ZnS quantum dots in Phanerochaete chrysosporium by cellular uptake and oxidative stress. *Environ. Sci.: Nano* **2017,** *4* (10), 2018-2029, DOI 10.1039/C7EN00517B.

17. Xiong, W.; Zeng, G.; Yang, Z.; Zhou, Y.; Zhang, C.; Cheng, M.; Liu, Y.; Hu, L.; Wan, J.; Zhou, C., Adsorption of tetracycline antibiotics from aqueous solutions on nanocomposite multi-walled carbon nanotube functionalized MIL-53 (Fe) as new adsorbent. *Sci. Total Environ.* **2018,** *627*, 235-244, DOI 10.1016/j.scitotenv.2018.01.249.

18. Zhang, C.; Liu, L.; Zeng, G.-M.; Huang, D.-L.; Lai, C.; Huang, C.; Wei, Z.; Li, N.-J.; Xu, P.; Cheng, M., Utilization of nano-gold tracing technique: study the adsorption and transmission of laccase in mediator-involved enzymatic degradation of lignin during solid-state fermentation. *Biochem. Eng. J.* **2014,** *91*, 149-156, DOI 10.1016/j.bej.2014.08.009.

19. Zhang, C.; Zeng, G.; Huang, D.; Lai, C.; Huang, C.; Li, N.; Xu, P.; Cheng, M.; Zhou, Y.; Tang, W., Combined removal of di (2-ethylhexyl) phthalate (DEHP) and Pb (II) by using a cutinase loaded nanoporous gold-polyethyleneimine adsorbent. *RSC Adv.* **2014,** *4* (98), 55511-55518, DOI 10.1039/C4RA09563D.

20. Zhang, C.; Lai, C.; Zeng, G.; Huang, D.; Tang, L.; Yang, C.; Zhou, Y.; Qin, L.; Cheng, M., Nanoporous Au-based chronocoulometric aptasensor for amplified detection of Pb^{2+} using DNAzyme modified with Au nanoparticles. *Biosens. Bioelectron.* **2016,** *81*, 61-67, DOI 10.1016/j.bios.2016.02.053.

21. Zhang, Y.; Zeng, G. M.; Tang, L.; Chen, J.; Zhu, Y.; He, X. X.; He, Y.,

Electrochemical Sensor Based on Electrodeposited Graphene-Au Modified Electrode and NanoAu Carrier Amplified Signal Strategy for Attomolar Mercury Detection. *Anal. Chem.* **2015,** *87* (2), 989-996, DOI 10.1021/ac503472p.

22. Cheng, M.; Zeng, G.; Huang, D.; Lai, C.; Liu, Y.; Zhang, C.; Wan, J.; Hu, L.; Zhou, C.; Xiong, W., Efficient degradation of sulfamethazine in simulated and real wastewater at slightly basic pH values using Co-SAM-SCS/H_2O_2 Fenton-like system. *Water Res.* **2018,** *138*, 7-18, DOI 10.1016/j.watres.2018.03.022.

23. Zeng, G.; Wan, J.; Huang, D.; Hu, L.; Huang, C.; Cheng, M.; Xue, W.; Gong, X.; Wang, R.; Jiang, D., Precipitation, adsorption and rhizosphere effect: The mechanisms for Phosphate-induced Pb immobilization in soils—A review. *J. Hazard. Mater.* **2017,** *339*, 354-367, DOI 10.1016/j.jhazmat.2017.05.038.

24. Xiong, W.; Tong, J.; Yang, Z.; Zeng, G.; Zhou, Y.; Wang, D.; Song, P.; Xu, R.; Zhang, C.; Cheng, M., Adsorption of phosphate from aqueous solution using iron-zirconium modified activated carbon nanofiber: Performance and mechanism. *J. Colloid Interface Sci.* **2017,** *493*, 17-23, DOI 10.1016/j.jcis.2017.01.024.

25. Zeng, G.; Zhang, C.; Huang, D.; Lai, C.; Tang, L.; Zhou, Y.; Xu, P.; Wang, H.; Qin, L.; Cheng, M., Practical and regenerable electrochemical aptasensor based on nanoporous gold and thymine-Hg^{2+}-thymine base pairs for Hg^{2+} detection. *Biosens. Bioelectron.* **2017,** *90*, 542-548, DOI 10.1016/j.bios.2016.10.018.

26. Li, B.; Lai, C.; Zeng, G.; Qin, L.; Yi, H.; Huang, D.; Zhou, C.; Liu, X.; Cheng, M.; Xu, P.; Zhang, C.; Huang, F.; Liu, S., Facile Hydrothermal Synthesis of Z-Scheme $Bi_2Fe_4O_9/Bi_2WO_6$ Heterojunction Photocatalyst with Enhanced Visible Light

Photocatalytic Activity. *ACS Appl. Mater. Interfaces* **2018,** *10* (22), 18824-18836, DOI 10.1021/acsami.8b06128.

27. Yang, Y.; Zhang, C.; Lai, C.; Zeng, G.; Huang, D.; Cheng, M.; Wang, J.; Chen, F.; Zhou, C.; Xiong, W., BiOX (X= Cl, Br, I) photocatalytic nanomaterials: Applications for fuels and environmental management. *Adv. Colloid Interface Sci.* **2018**, 254, 76-93, DOI 10.1016/j.cis.2018.03.004.

28. Dong, H.; Zeng, G.; Tang, L.; Fan, C.; Zhang, C.; He, X.; He, Y., An overview on limitations of TiO_2-based particles for photocatalytic degradation of organic pollutants and the corresponding countermeasures. *Water Res.* **2015,** *79*, 128-146, DOI 10.1016/j.watres.2015.04.038.

29. Vaiano, V.; Matarangolo, M.; Murcia, J. J.; Rojas, H.; Navío, J. A.; Hidalgo, M. C., Enhanced photocatalytic removal of phenol from aqueous solutions using ZnO modified with Ag. *Appl. Catal., B* **2018,** *225*, 197-206, DOI 10.1016/j.apcatb.2017.11.075.

30. Zhou, X.; Lai, C.; Huang, D.; Zeng, G.; Chen, L.; Qin, L.; Xu, P.; Cheng, M.; Huang, C.; Zhang, C., Preparation of water-compatible molecularly imprinted thiol-functionalized activated titanium dioxide: Selective adsorption and efficient photodegradation of 2, 4-dinitrophenol in aqueous solution. *J. Hazard. Mater.* **2018,** *346*, 113-123, DOI 10.1016/j.jhazmat.2017.12.032.

31. Lai, C.; Wang, M.-M.; Zeng, G.-M.; Liu, Y.-G.; Huang, D.-L.; Zhang, C.; Wang, R.-Z.; Xu, P.; Cheng, M.; Huang, C., Synthesis of surface molecular imprinted TiO_2/graphene photocatalyst and its highly efficient photocatalytic degradation of

target pollutant under visible light irradiation. *Appl. Surf. Sci.* **2016,** *390*, 368-376, DOI 10.1016/j.apsusc.2016.08.119.

32. Zhou, C.; Lai, C.; Huang, D.; Zeng, G.; Zhang, C.; Cheng, M.; Hu, L.; Wan, J.; Xiong, W.; Wen, M.; Wen, X.; Qin, L., Highly porous carbon nitride by supramolecular preassembly of monomers for photocatalytic removal of sulfamethazine under visible light driven. *Appl. Catal., B* **2018,** *220*, 202-210, DOI 10.1016/j.apcatb.2017.08.055.

33. Cao, Y.; Zhang, Z.; Long, J.; Liang, J.; Lin, H.; Lin, H.; Wang, X., Vacuum heat-treatment of carbon nitride for enhancing photocatalytic hydrogen evolution. J. Mater. Chem. A **2014,** 2 (42), 17797-17807, DOI 10.1039/C4TA03070B.

34. Wang, X.; Maeda, K.; Thomas, A.; Takanabe, K.; Xin, G.; Carlsson, J. M.; Domen, K.; Antonietti, M., A metal-free polymeric photocatalyst for hydrogen production from water under visible light. *Nat. Mater.* **2009,** *8* (1), 76-80, DOI 10.1038/nmat2317.

35. Tian, N.; Zhang, Y.; Li, X.; Xiao, K.; Du, X.; Dong, F.; Waterhouse, G. I. N.; Zhang, T.; Huang, H., Precursor-reforming protocol to 3D mesoporous g-C_3N_4 established by ultrathin self-doped nanosheets for superior hydrogen evolution. *Nano Energy* **2017,** *38*, 72-81, DOI 10.1016/j.nanoen.2017.05.038.

36. Gu, Q.; Liao, Y.; Yin, L.; Long, J.; Wang, X.; Xue, C., Template-free synthesis of porous graphitic carbon nitride microspheres for enhanced photocatalytic hydrogen generation with high stability. *Appl. Catal., B* **2015,** *165*, 503-510, DOI 10.1016/j.apcatb.2014.10.045.

37. Liu, J.; Jia, Q.; Long, J.; Wang, X.; Gao, Z.; Gu, Q., Amorphous NiO as co-catalyst for enhanced visible-light-driven hydrogen generation over g-C_3N_4 photocatalyst. *Appl. Catal., B* **2018,** *222*, 35-43, DOI 10.1016/j.apcatb.2017.09.073.

38. Huang, H.; Xiao, K.; Tian, N.; Dong, F.; Zhang, T.; Du, X.; Zhang, Y., Template-free precursor-surface-etching route to porous, thin g-C_3N_4 nanosheets for enhancing photocatalytic reduction and oxidation activity. *J. Mater. Chem. A* **2017,** *5* (33), 17452-17463, DOI 10.1039/C7TA04639A.

39. Jiang, L.; Yuan, X.; Pan, Y.; Liang, J.; Zeng, G.; Wu, Z.; Wang, H., Doping of graphitic carbon nitride for photocatalysis: A reveiw. *Appl. Catal., B* **2017,** *217*, 388-406, DOI 10.1016/j.apcatb.2017.06.003.

40. Ding, F.; Yang, D.; Tong, Z.; Nan, Y.; Wang, Y.; Zou, X.; Jiang, Z., Graphitic carbon nitride-based nanocomposites as visible-light driven photocatalysts for environmental purification. *Environ. Sci.: Nano* **2017,** *4* (7), 1455-1469, DOI 10.1039/C7EN00255F.

41. Wang, H.; Yuan, X.; Wang, H.; Chen, X.; Wu, Z.; Jiang, L.; Xiong, W.; Zeng, G., Facile synthesis of Sb_2S_3/ultrathin g-C_3N_4 sheets heterostructures embedded with g-C_3N_4 quantum dots with enhanced NIR-light photocatalytic performance. *Appl. Catal., B* **2016,** *193*, 36-46, DOI 10.1016/j.apcatb.2016.03.075.

42. Wang, J.; Tang, L.; Zeng, G.; Deng, Y.; Liu, Y.; Wang, L.; Zhou, Y.; Guo, Z.; Wang, J.; Zhang, C., Atomic scale g-C_3N_4/Bi_2WO_6 2D/2D heterojunction with enhanced photocatalytic degradation of ibuprofen under visible light irradiation. *Appl. Catal., B* **2017,** *209*, 285-294, DOI 10.1016/j.apcatb.2017.03.019.

43. Wang, F.; Feng, Y.; Chen, P.; Wang, Y.; Su, Y.; Zhang, Q.; Zeng, Y.; Xie, Z.; Liu, H.; Liu, Y.; Lv, W.; Liu, G., Photocatalytic degradation of fluoroquinolone antibiotics using ordered mesoporous g-C_3N_4 under simulated sunlight irradiation: Kinetics, mechanism, and antibacterial activity elimination. *Appl. Catal., B* **2018,** *227*, 114-122, DOI 10.1016/j.apcatb.2018.01.024.

44. Guo, Y.; Chen, T.; Liu, Q.; Zhang, Z.; Fang, X., Insight into the Enhanced Photocatalytic Activity of Potassium and Iodine Codoped Graphitic Carbon Nitride Photocatalysts. *J. Physi. Chem. C* **2016,** *120* (44), 25328-25337, DOI 10.1021/acs.jpcc.6b06921.

45. Bao, N.; Hu, X.; Zhang, Q.; Miao, X.; Jie, X.; Zhou, S., Synthesis of porous carbon-doped g-C_3N_4 nanosheets with enhanced visible-light photocatalytic activity. *Appl. Surf. Sci.* **2017,** *403*, 682-690, DOI *10.*1016/j.apsusc.2017.01.256.

46. Fang, L. J.; Wang, X. L.; Zhao, J. J.; Li, Y. H.; Wang, Y. L.; Du, X. L.; He, Z. F.; Zeng, H. D.; Yang, H. G., One-step fabrication of porous oxygen-doped g-C_3N_4 with feeble nitrogen vacancies for enhanced photocatalytic performance. *Chem. Commun.* **2016,** *52* (100), 14408-14411, DOI 10.1039/C6CC08187H.

47. Zhu, Y. P.; Ren, T. Z.; Yuan, Z. Y., Mesoporous Phosphorus-Doped g-C_3N_4 Nanostructured Flowers with Superior Photocatalytic Hydrogen Evolution Performance. *ACS Appl. Mater. Interfaces* **2015,** *7* (30), 16850-16856, DOI 10.1021/acsami.5b04947.

48. Zhang, Z.; Long, J.; Yang, L.; Chen, W.; Dai, W.; Fu, X.; Wang, X., Organic semiconductor for artificial photosynthesis: water splitting into hydrogen by a

bioinspired $C_3N_3S_3$ polymer under visible light irradiation. *Chem. Sci.* **2011,** *2* (9), 1826-1830, DOI 10.1039/C1SC00257K.

49. Yi, H.; Huang, D.; Qin, L.; Zeng, G.; Lai, C.; Cheng, M.; Ye, S.; Song, B.; Ren, X.; Guo, X., Selective prepared carbon nanomaterials for advanced photocatalytic application in environmental pollutant treatment and hydrogen production. *Appl. Catal., B* **2018,** *239*, 408-424, DOI 10.1016/j.apcatb.2018.07.068.

50. Sun, X.; Jiang, D.; Zhang, L.; Wang, W., Alkaline modified g-C_3N_4photocatalyst for high selective oxide coupling of benzyl alcohol to benzoin. *Appl. Catal., B* **2018,** *220*, 553-560, DOI 10.1016/j.apcatb.2017.08.057.

51. Zhou, S.; Liu, Y.; Li, J.; Wang, Y.; Jiang, G.; Zhao, Z.; Wang, D.; Duan, A.; Liu, J.; Wei, Y., Facile in situ synthesis of graphitic carbon nitride (g-C_3N_4)-N-TiO_2 heterojunction as an efficient photocatalyst for the selective photoreduction of CO_2 to CO. *Appl. Catal., B* **2014,** *158-159*, 20-29, DOI 10.1016/j.apcatb.2014.03.037.

52. Zhang, M.; Bai, X.; Liu, D.; Wang, J.; Zhu, Y., Enhanced catalytic activity of potassium-doped graphitic carbon nitride induced by lower valence position. *Appl. Catal., B* **2015,** *164*, 77-81, DOI 10.1016/j.apcatb.2014.09.020.

53. Zhou, C.; Lai, C.; Xu, P.; Zeng, G.; Huang, D.; Li, Z.; Zhang, C.; Cheng, M.; Hu, L.; Wan, J.; Chen, F.; Xiong, W.; Deng, R., Rational Design of Carbon-Doped Carbon Nitride/$Bi_{12}O_{17}Cl_2$ Composites: A Promising Candidate Photocatalyst for Boosting Visible-Light-Driven Photocatalytic Degradation of Tetracycline. *ACS Sustainable Chem. Eng.* **2018,** 6 (5), 6941-6949, DOI 10.1021/acssuschemeng.8b00782.

54. Chang, C.; Zhu, L.; Wang, S.; Chu, X.; Yue, L., Novel mesoporous graphite

carbon nitride/BiOI heterojunction for enhancing photocatalytic performance under visible-light irradiation. *ACS Appl. Mater. Interfaces* **2014,** *6* (7), 5083-5093, DOI 10.1021/am5002597.

55. Fang, W.; Liu, J.; Yu, L.; Jiang, Z.; Shangguan, W., Novel (Na, O) co-doped g-C_3N_4 with simultaneously enhanced absorption and narrowed bandgap for highly efficient hydrogen evolution. *Appl. Catal., B* **2017,** *209*, 631-636, DOI 10.1016/j.apcatb.2017.03.041.

56. Sun, Z.; Fischer, J. M. T. A.; Li, Q.; Hu, J.; Tang, Q.; Wang, H.; Wu, Z.; Hankel, M.; Searles, D. J.; Wang, L., Enhanced CO_2 photocatalytic reduction on alkali-decorated graphitic carbon nitride. *Appl. Catal., B* **2017,** *216*, 146-155, DOI 10.1016/j.apcatb.2017.05.064.

57. Wang, J.; Tang, L.; Zeng, G.; Deng, Y.; Dong, H.; Liu, Y.; Wang, L.; Peng, B.; Zhang, C.; Chen, F., 0D/2D interface engineering of carbon quantum dots modified Bi_2WO_6 ultrathin nanosheets with enhanced photoactivity for full spectrum light utilization and mechanism insight. Appl. Catal., B 2018, 222, 115-123, DOI 10.1016/j.apcatb.2017.10.014.

58. Hu, S.; Li, F.; Fan, Z.; Wang, F.; Zhao, Y.; Lv, Z., Band gap-tunable potassium doped graphitic carbon nitride with enhanced mineralization ability. *Dalton Trans.* **2015,** *44* (3), 1084-1092, DOI 10.1039/C4DT02658F.

59. Xiong, T.; Cen, W.; Zhang, Y.; Dong, F., Bridging the g-C_3N_4 Interlayers for Enhanced Photocatalysis. *ACS Catal.* **2016,** *6* (4), 2462-2472, DOI 10.1021/acscatal.5b02922.

60. Guo, F.; Chen, J.; Zhang, M.; Gao, B.; Lin, B.; Chen, Y., Deprotonation of g-C_3N_4 with Na ions for efficient nonsacrificial water splitting under visible light. *J. Mater. Chem. A* **2016,** *4* (28), 10806-10809, DOI 10.1039/C6TA03424A.

61. Yuan, X.; Zhou, C.; Jin, Y.; Jing, Q.; Yang, Y.; Shen, X.; Tang, Q.; Mu, Y.; Du, A. K., Facile synthesis of 3D porous thermally exfoliated g-C_3N_4 nanosheet with enhanced photocatalytic degradation of organic dye. *J. Colloid Interface Sci.* **2016,** *468*, 211-219, DOI 10.1016/j.jcis.2016.01.048.

62. Jiang, L.; Yuan, X.; Zeng, G.; Chen, X.; Wu, Z.; Liang, J.; Zhang, J.; Wang, H.; Wang, H., Phosphorus- and Sulfur-Codoped g-C_3N_4: Facile Preparation, Mechanism Insight, and Application as Efficient Photocatalyst for Tetracycline and Methyl Orange Degradation under Visible Light Irradiation. ACS Sustainable Chem. Eng. 2017, 5 (7), 5831-5841, DOI 10.1021/acssuschemeng.7b00559.

63. Zhou, C.; Lai, C.; Zhang, C.; Zeng, G.; Huang, D.; Cheng, M.; Hu, L.; Xiong, W.; Chen, M.; Wang, J.; Yang, Y.; Jiang, L., Semiconductor/boron nitride composites: Synthesis, properties, and photocatalysis applications. Appl. Catal., B 2018, 238, 6-18, DOI 10.1016/j.apcatb.2018.07.011.

64. Li, H.; Yu, H.; Quan, X.; Chen, S.; Zhang, Y., Uncovering the Key Role of the Fermi Level of the Electron Mediator in a Z-Scheme Photocatalyst by Detecting the Charge Transfer Process of WO_3-metal- g-C_3N_4 (Metal = Cu, Ag, Au). *ACS Appl. Mater. Interfaces* **2016,** *8* (3), 2111-2119, DOI 10.1021/acsami.5b10613.

65. Zhou, C.; Lai, C.; Xu, P.; Zeng, G.; Huang, D.; Zhang, C.; Cheng, M.; Hu, L.; Wan, J.; Liu, Y.; Xiong, W.; Deng, Y.; Wen, M., In Situ Grown AgI/$Bi_{12}O_{17}Cl_2$

Heterojunction Photocatalysts for Visible Light Degradation of Sulfamethazine: Efficiency, Pathway, and Mechanism. *ACS Sustainable Chem. Eng.* **2018,** *6* (3), 4174-4184, DOI 10.1021/acssuschemeng.7b04584.

66. Guo, H.; Niu, C. G.; Wen, X. J.; Zhang, L.; Liang, C.; Zhang, X. G.; Guan, D. L.; Tang, N.; Zeng, G. M., Construction of highly efficient and stable ternary AgBr/Ag/$PbBiO_2Br$ Z-scheme photocatalyst under visible light irradiation: Performance and mechanism insight. *J. Colloid Interface Sci.* **2018,** *513*, 852-865, DOI 10.1016/j.jcis.2017.12.010.

67. Yang, Y.; Zeng, Z.; Zhang, C.; Huang, D.; Zeng, G.; Xiao, R.; Lai, C.; Zhou, C.; Guo, H.; Xue, W.; Cheng, M.; Wang, W.; Wang, J., Construction of iodine vacancy-rich BiOI/Ag@AgI Z-scheme heterojunction photocatalysts for visible-light-driven tetracycline degradation: Transformation pathways and mechanism insight. *Chem. Eng. J.* **2018,** *349*, 808-821, DOI 10.1016/j.cej.2018.05.093.

68. Chen, F.; Yang, Q.; Li, X.; Zeng, G.; Wang, D.; Niu, C.; Zhao, J.; An, H.; Xie, T.; Deng, Y., Hierarchical assembly of graphene-bridged Ag_3PO_4/Ag/$BiVO_4$ (040) Z-scheme photocatalyst: An efficient, sustainable and heterogeneous catalyst with enhanced visible-light photoactivity towards tetracycline degradation under visible light irradiation. *Appl. Catal., B* **2017,** *200*, 330-342, DOI 10.1016/j.apcatb.2016.07.021.

69. Chen, F.; Yang, Q.; Sun, J.; Yao, F.; Wang, S.; Wang, Y.; Wang, X.; Li, X.; Niu, C.; Wang, D.; Zeng, G., Enhanced Photocatalytic Degradation of Tetracycline by

AgI/$BiVO_4$ Heterojunction under Visible-Light Irradiation: Mineralization Efficiency and Mechanism. *ACS Appl. Mater. Interfaces* **2016,** *8* (48), 32887-32900, DOI 10.1021/acsami.6b12278.

70. Deng, Y.; Tang, L.; Zeng, G.; Feng, C.; Dong, H.; Wang, J.; Feng, H.; Liu, Y.; Zhou, Y.; Pang, Y., Plasmonic resonance excited dual Z-scheme $BiVO_4$/Ag/Cu_2O nanocomposite: synthesis and mechanism for enhanced photocatalytic performance in recalcitrant antibiotic degradation. *Environ. Sci.: Nano* **2017,** *4* (7), 1494-1511, DOI 10.1039/C7EN00237H.

71. Cao, J.; Yang, Z.-h.; Xiong, W.-p.; Zhou, Y.-y.; Peng, Y.; Li, X.; Zhou, C.-y.; Xu, R.; Zhang, Y.-r., One-step synthesis of Co-doped UiO-66 nanoparticle with enhanced removal efficiency of tetracycline: Simultaneous adsorption and photocatalysis. *Chem. Eng. J.* **2018,** *353*, 126-137, DOI 10.1016/j.cej.2018.07.060.

72. Guo, H.; Niu, C.-G.; Zhang, L.; Wen, X.-J.; Liang, C.; Zhang, X.-G.; Guan, D.-L.; Tang, N.; Zeng, G.-M., Construction of Direct Z-Scheme AgI/$Bi_2Sn_2O_7$ Nanojunction System with Enhanced Photocatalytic Activity: Accelerated Interfacial Charge Transfer Induced Efficient Cr(VI) Reduction, Tetracycline Degradation and Escherichia coli Inactivation. *ACS Sustainable Chem. Eng.* **2018,** *6* (6), 8003-8018, DOI 10.1021/acssuschemeng.8b01448.

73. Chen, Y.-Y.; Ma, Y.-L.; Yang, J.; Wang, L.-Q.; Lv, J.-M.; Ren, C.-J., Aqueous tetracycline degradation by H_2O_2 alone: Removal and transformation pathway. *Chem. Eng. J.* **2017,** *307*, 15-23, DOI 10.1016/j.cej.2016.08.046.

74. Cao, J.; Xiong, Z.; Lai, B., Effect of initial pH on the tetracycline (TC) removal

by zero-valent iron: Adsorption, oxidation and reduction. *Chem. Eng. J.* **2018,** *343*, 492-499, DOI 10.1016/j.cej.2018.03.036.

75. Zhuang, H.; Yang, L.; Xu, J.; Li, F.; Zhang, Z.; Lin, H.; Long, J.; Wang, X., Robust Photocatalytic H_2O_2 Production by Octahedral $Cd_3(C_3N_3S_3)_2$ Coordination Polymer under Visible Light. *Sci. Rep.* **2015,** *5*, 16947, DOI 10.1038/srep16947.

76. Xu, J.; Chen, Z.; Zhang, H.; Lin, G.; Lin, H.; Wang, X.; Long, J., $Cd_3(C_3N_3S_3)_2$ coordination polymer/graphene nanoarchitectures for enhanced photocatalytic H_2O_2 production under visible light. *Sci. Bull.* **2017,** *62* (9), 610-618, DOI 10.1016/j.scib.2017.04.013.

Table 1

Surface area, pore volume and pore size parameters for bulk g-C_3N_4, MCN and KMCN (x) x=0, 0.02, 0.05, 0.1 and 0.2.

Samples	Surface area[1] (m^2/g)	Pore volume[2] (cm^3/g)	Pore size[3] (nm)
g-C_3N_4	12.735	0.073	19.676
MCN	26.566	0.149	21.422
KMCN (0)	29.314	0.159	23.275
KMCN (0.02)	34.155	0.207	22.410
KMCN (0.05)	50.196	0.321	27.784
KMCN (0.1)	42.792	0.253	23.217
KMCN (0.2)	40.983	0.240	21.288

[1] Measured using N_2 adsorption with Brunauer-Emmett-Teller (BET) method.

[2] Single point adsorption total pore volume of pores determined at P/P_o = 0.99.

[3] Average pore size by the desorption data via Barrett-Joyner-Halenda (BJH) method.

Table 2

Degradation efficiencies (DE), Pseudo--first-order rate constants (K_{app}) and standard error for the TC

Photocatalyst	K_{app}/min^{-1}	Standard error	DE (%)
g-C_3N_4	0.0058	0.0005	29.60
MCN	0.0161	0.0013	60.84
KMCN (0)	0.0177	0.0039	67.91
KMCN (0.02)	0.0195	0.0047	71.66
KMCN (0.05)	0.0282	0.0084	85.13
KMCN (0.1)	0.0233	0.0082	80.18
KMCN (0.2)	0.0209	0.0076	75.49

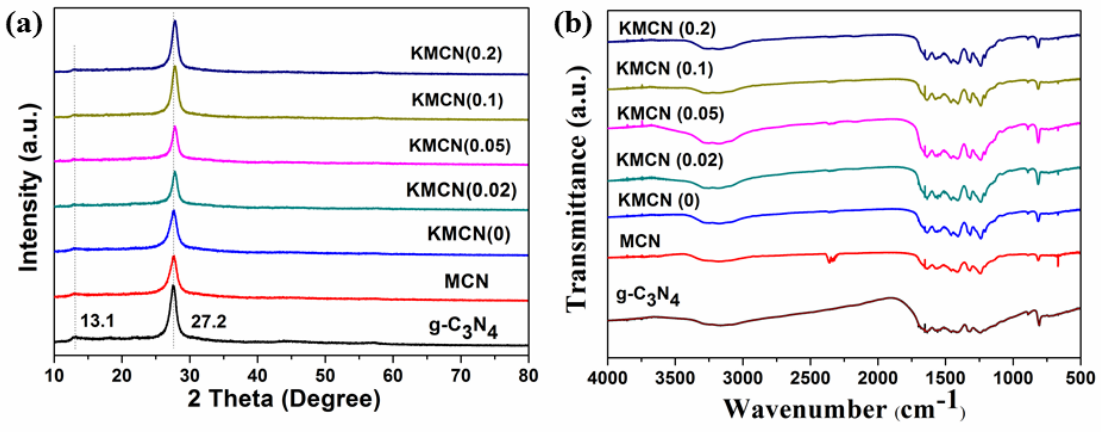

Figure 1. (a) The XRD patterns and (b) the FT-IR spectra of samples bulk g-C_3N_4, MCN and KMCN (x) x=0, 0.02, 0.05, 0.1 and 0.2.

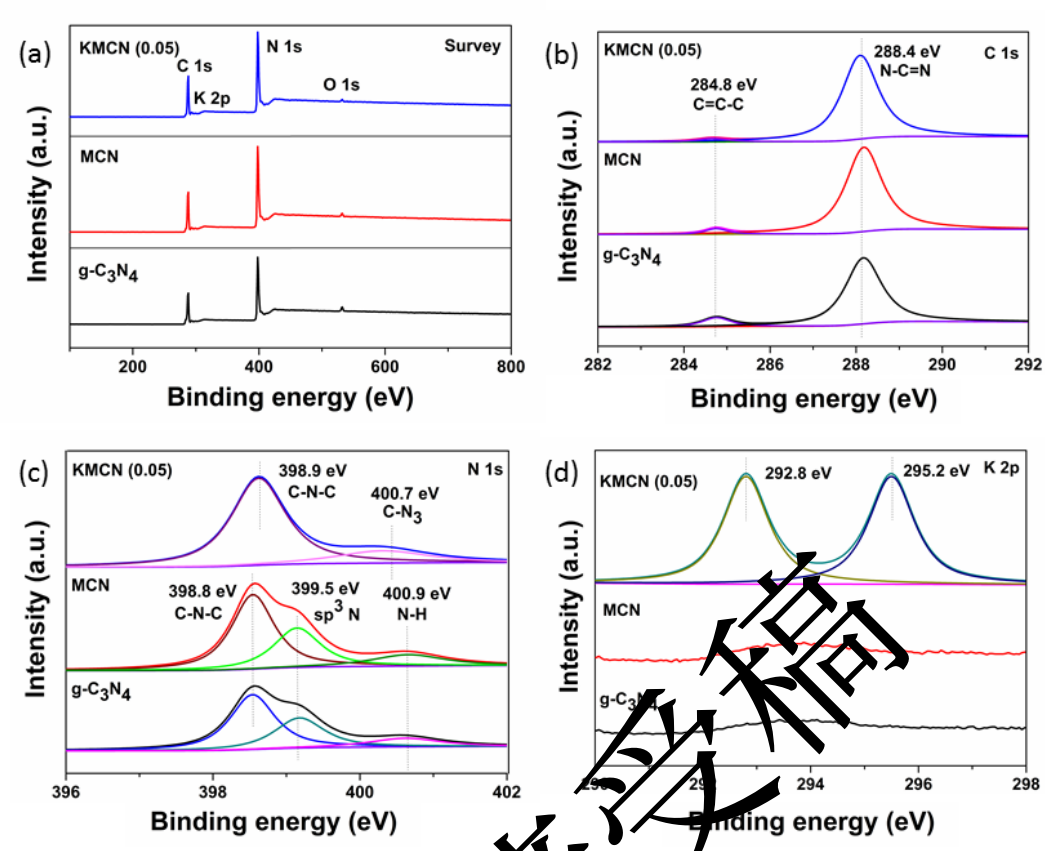

Figure 2. XPS spectra of samples bulk $g\text{-}C_3N_4$, MCN and KMCN (0.05) survey spectra (a), high resolution C 1s region (b), N 1s region (c) and K 2p region (d).

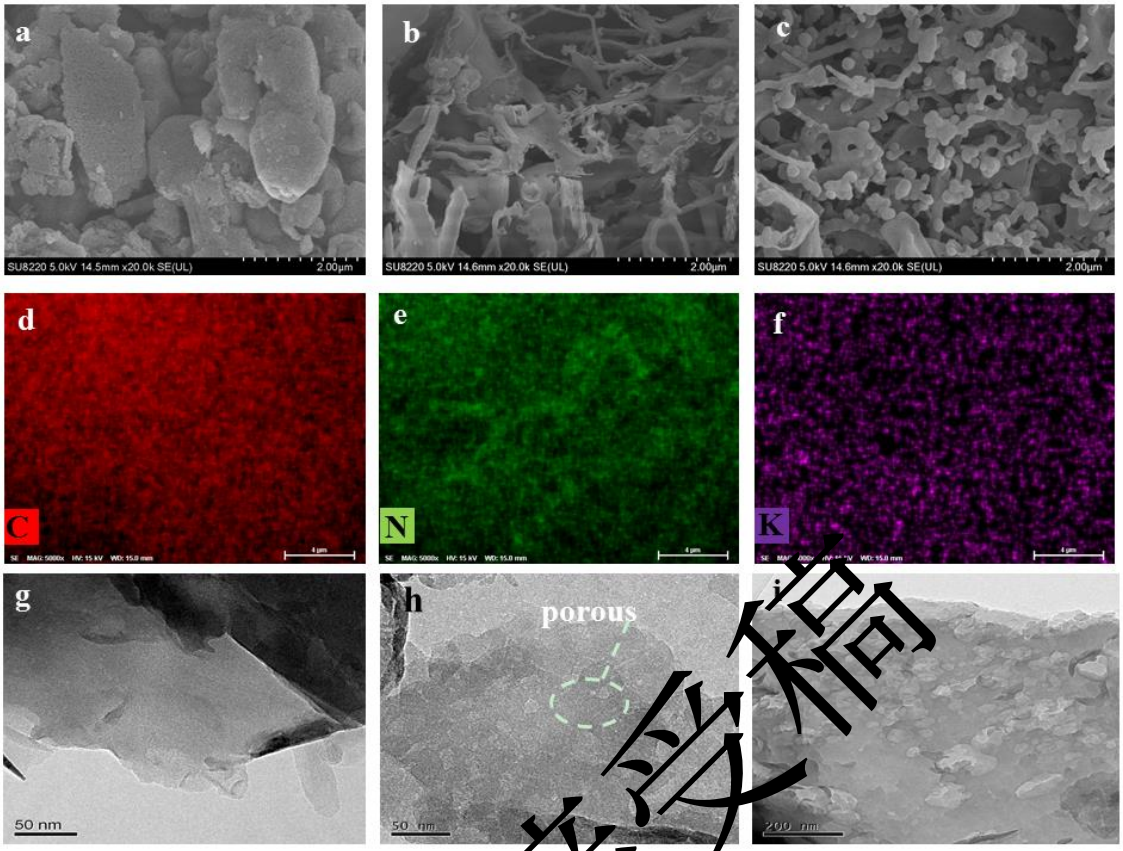

Figure 3. The SEM images of samples: (a) bulk g-C_3N_4, (b) MCN and (c) KMCN (0.05). EDS element mapping images for (d) C, (e) N and (f) K in the KMCN (0.05). The TEM images of as-prepared photocatalysts: (g) bulk g-C_3N_4, (h) MCN, (i) KMCN (0.05).

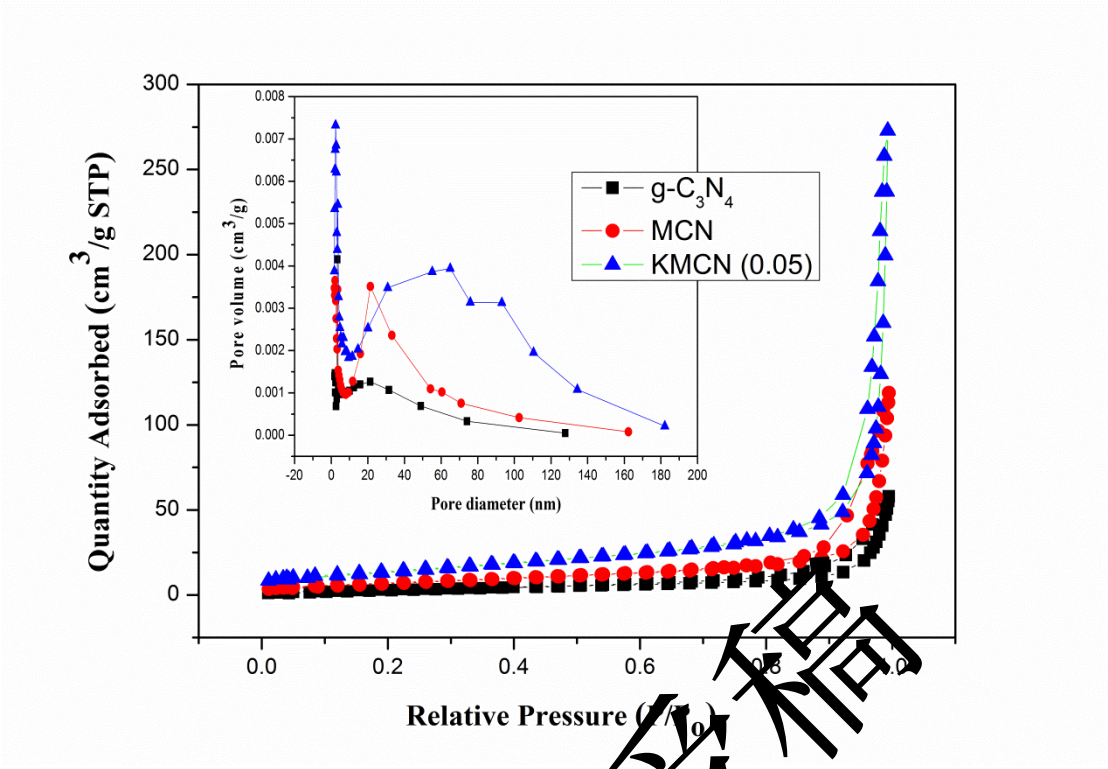

Figure 4. N_2 adsorption−desorption isotherms of the prepared materials bulk g-C_3N_4, MCN and KMCN (0.05). Inset: The pore size distributions were determined from the desorption branch of the isotherm.

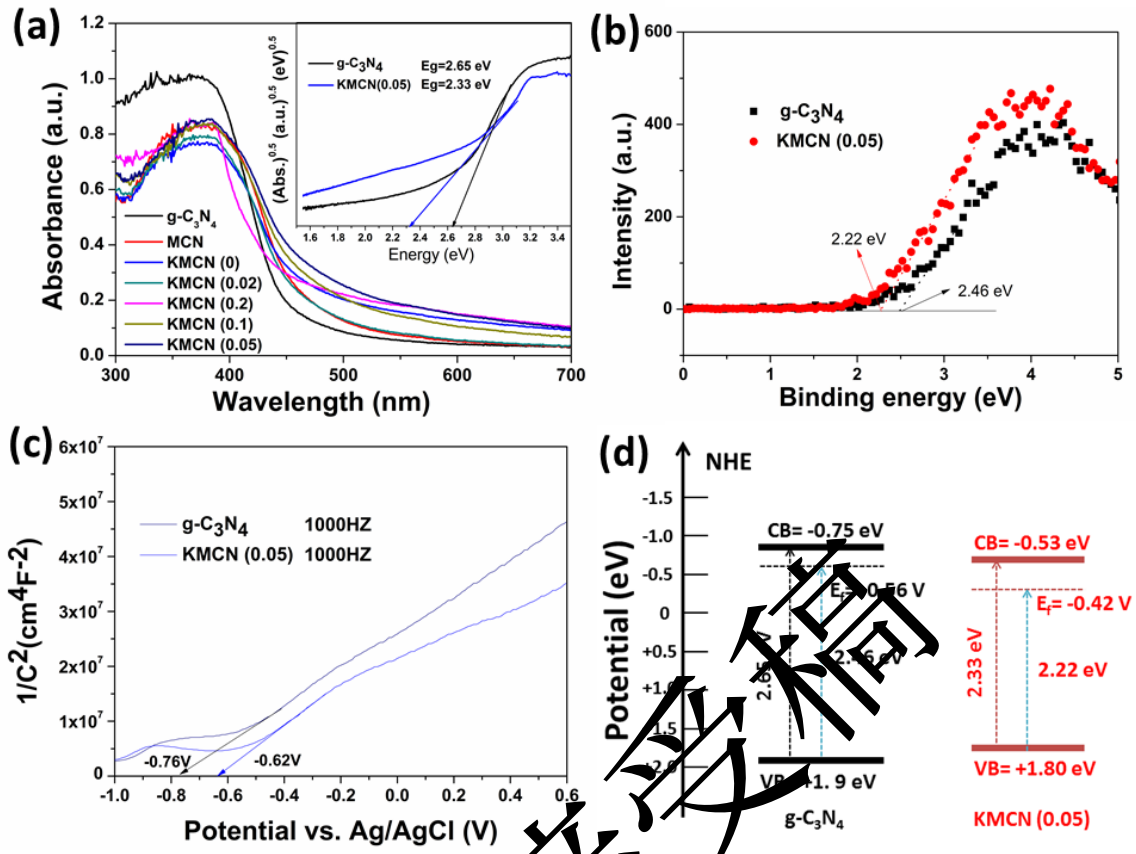

Figure 5. (a) UV-Vis reflectance spectra of samples; and (inset figure) band gap of bulk g-C_3N_4 and KMCN (0.05); (b) Valence band XPS spectra, (c) Mott–Schottky plots and (d) band structure diagram of bulk g-C_3N_4 and KMCN (0.05).

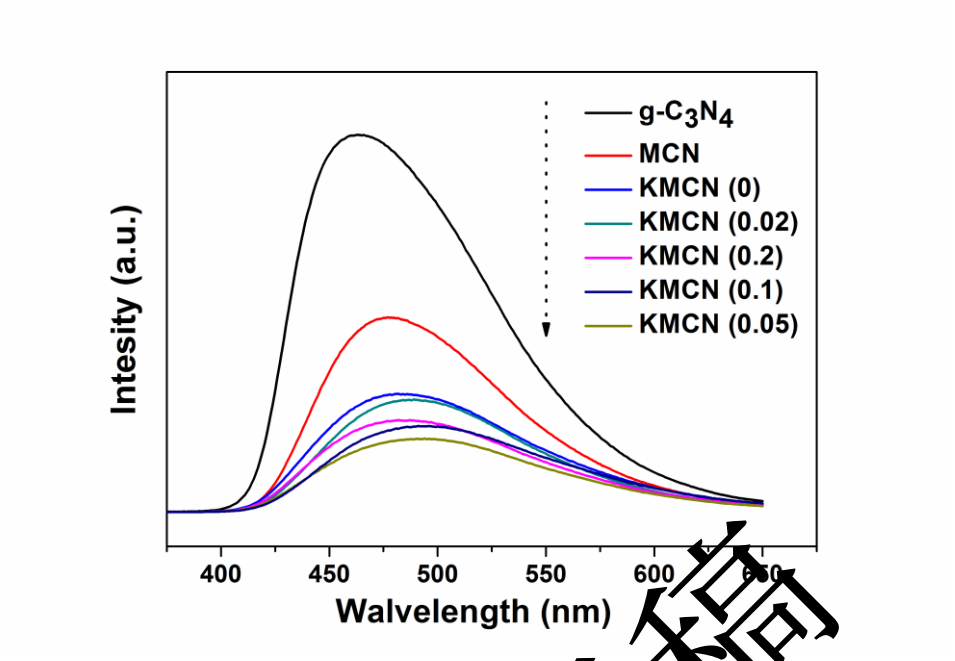

Figure 6. Photoluminescence spectra of samples bulk $g\text{-}C_3N_4$, MCN and KMCN (x) x=0, 0.02, 0.05, 0.1 and 0.2.

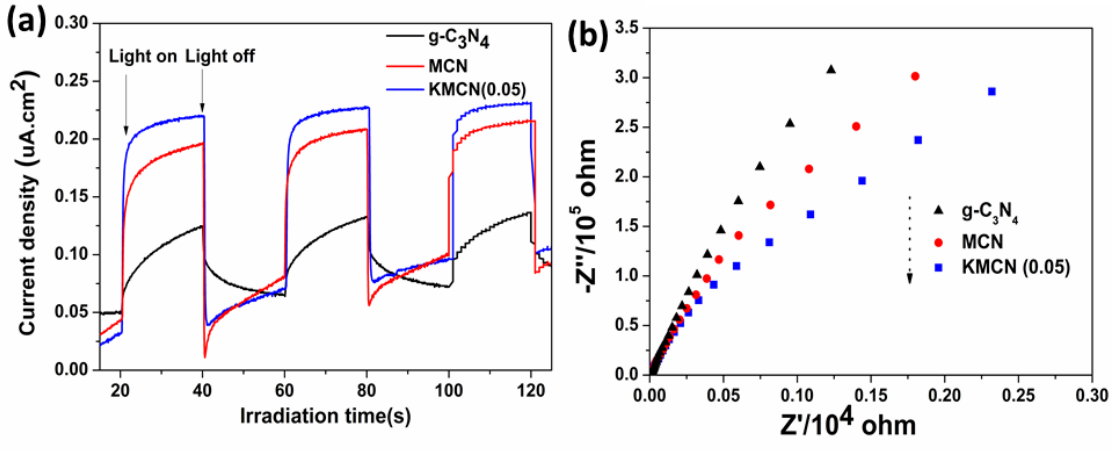

Figure 7. (a) Photocurrent response spectra and (b) electrochemical impedance spectra (EIS) of bulk g-C_3N_4, MCN and KMCN (0.05) catalysts.

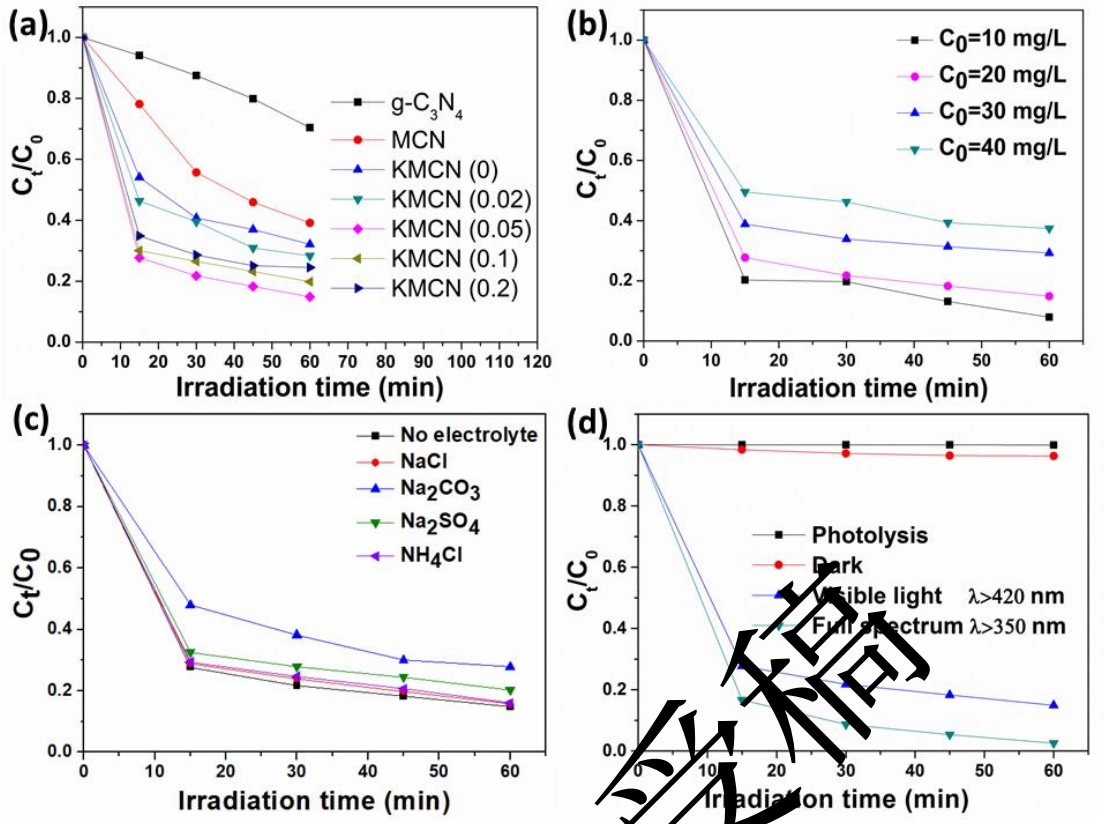

Figure 8. (a) Photocatalytic degradation of TC over as-prepared samples. And effects of (b) initial TC concentrations; (c) supporting electrolytes and (d) different light irradiation conditions on the degradation of TC over KMCN (0.05) catalysts. Each data was an average of three replicate determinations.

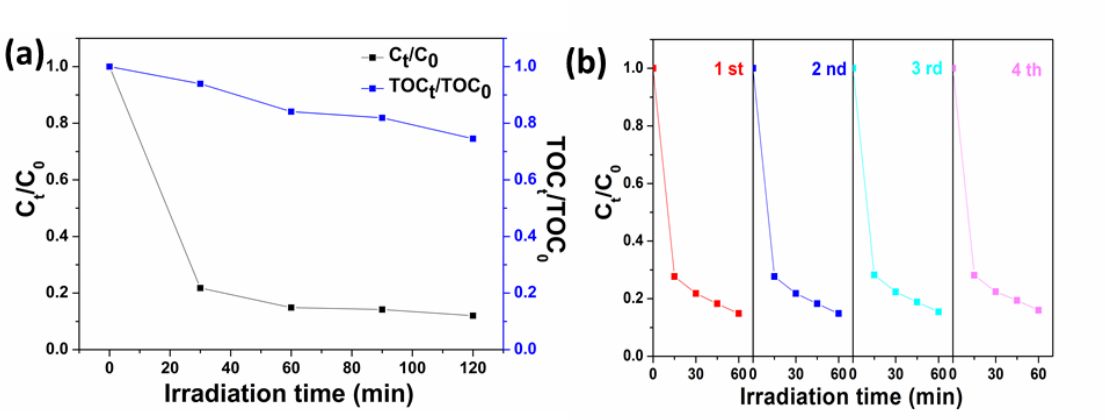

Figure 9. (a) The photocatalytic degradation and TOC removal curves of TC on KMCN (0.05) catalysts; (b) The cycling test for degradation of TC by the fresh and used KMCN (0.05) catalysts.

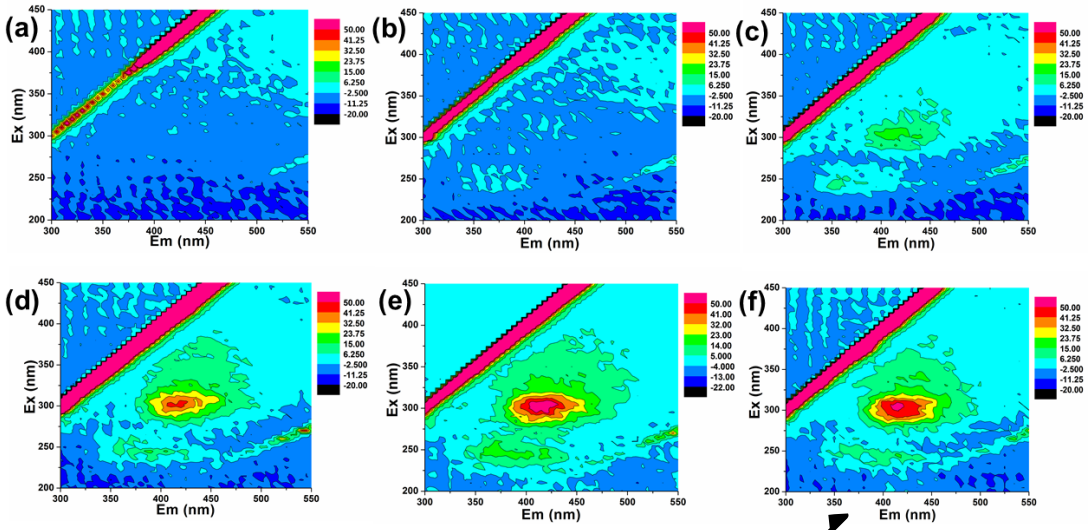

Figure 10. 3D EEMs results of (a) original TC aqueous solution, (b) TC solution obtained from 1 h adsorption process in dark, and (c-f) TC solution collected after visible light irradiation time of 0.5, 1, 1.5 and 2 h, respectively.

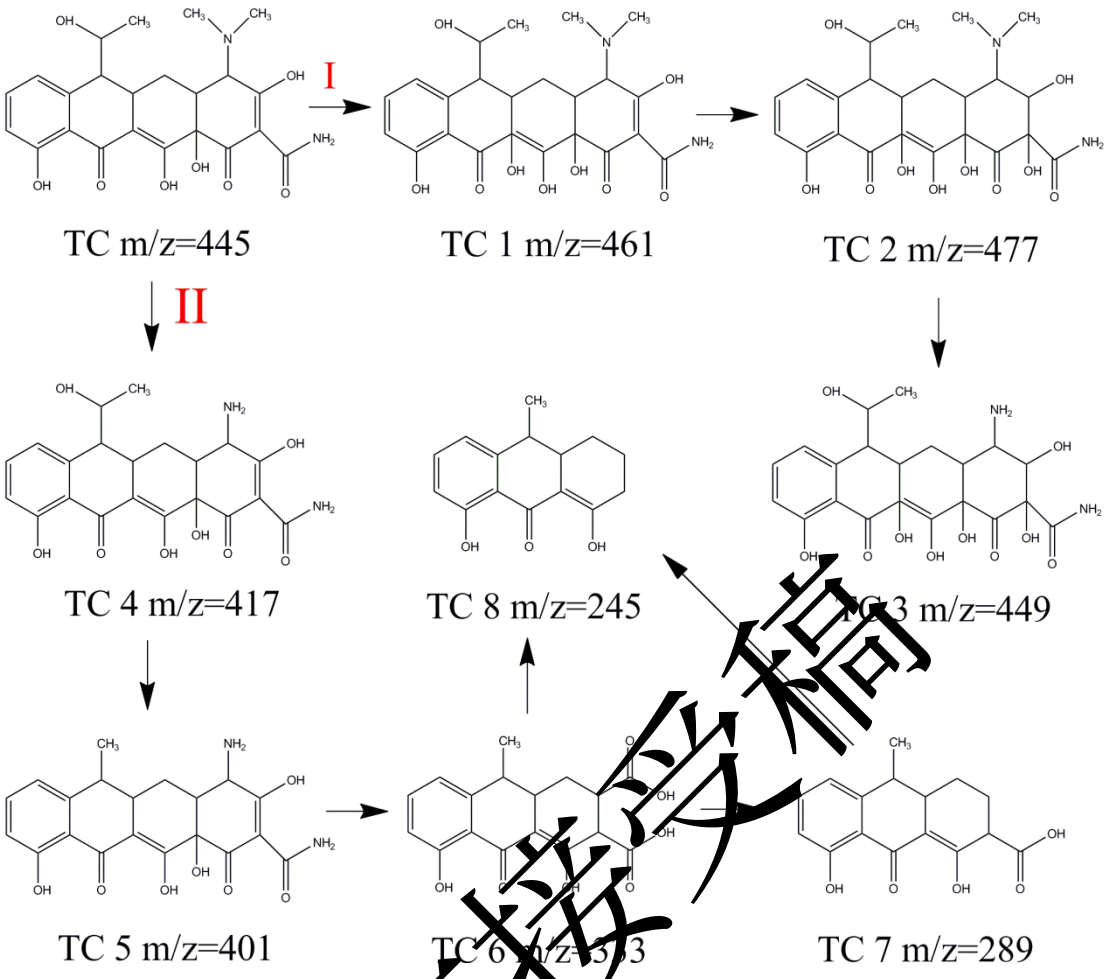

Figure 11. Proposed degradation pathway of TC and the chemical structure of intermediates.

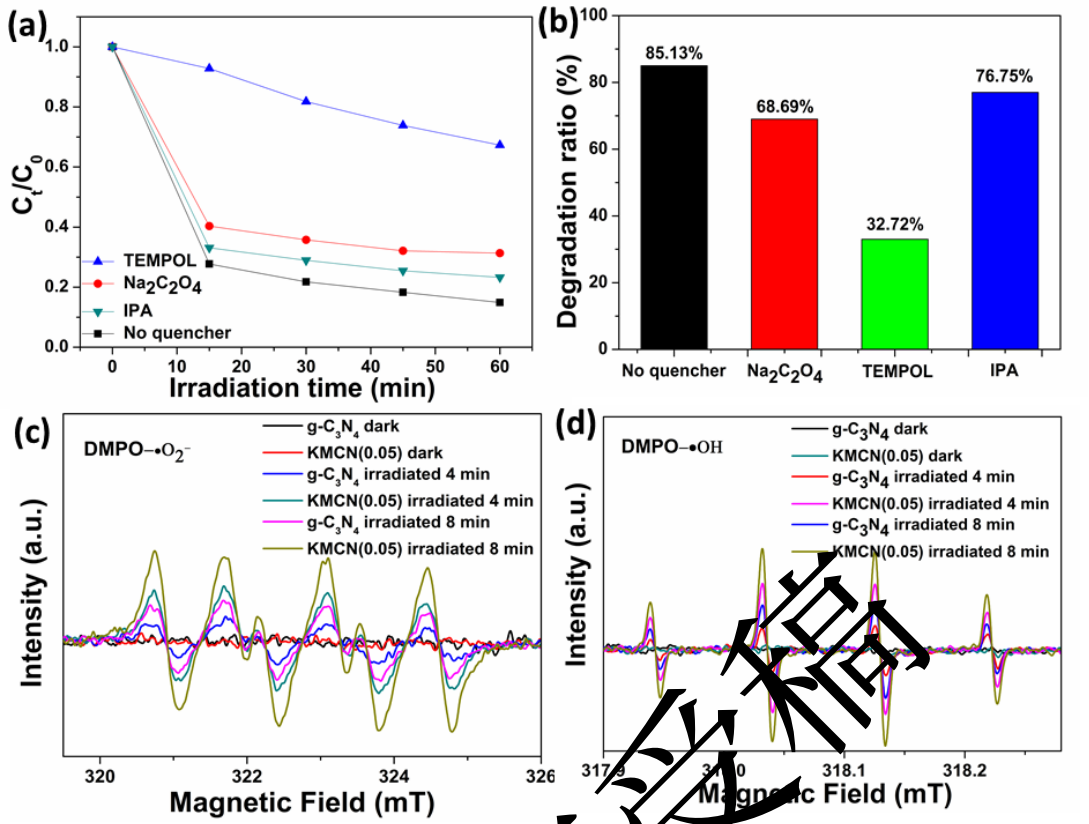

Figure 12. (a, b) Photocatalytic activities of the KMCN (0.05) sample for the degradation of TC under the condition of different quenchers. ESR spectra of radical adducts tapped by DMPO spin-trapping in bulk g-C_3N_4 and KMCN (0.05) dispersion in the dark and under visible light irradiation (irradiation time of 4 and 8 minute): (c) in methanol dispersion for DMPO-•O_2^-; (d) in aqueous dispersion for DMPO-•OH.

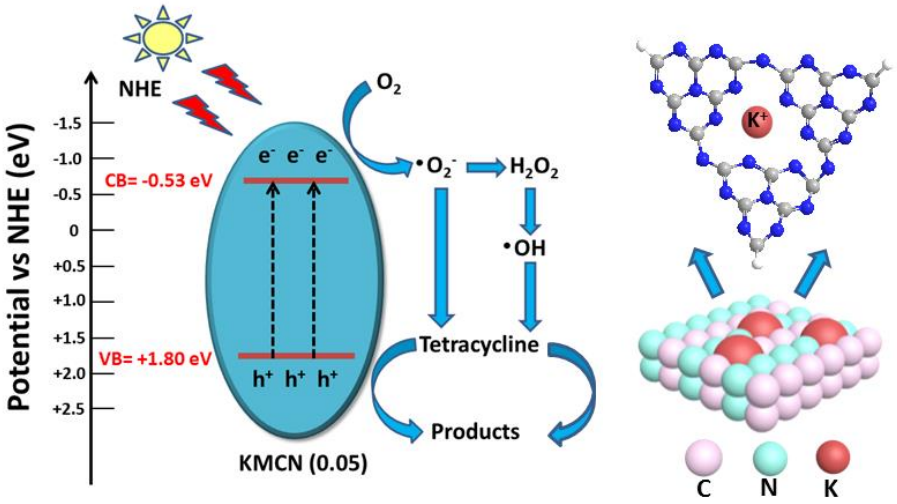

Scheme 1. The possible photocatalytic mechanism scheme of KMCN (0.05) composite for the photo-degradation of tetracycline under visible light irradiation.